Modulating electronic structure of lattice O-modified orange polymeric carbon nitrogen to promote photocatalytic CO_2 conversion

Jinman Yang [a], Liquan Jing [a], Xingwang Zhu [b], Wei Zhang [a], Jiujun Deng [a], Yuanbin She [c,*], Kaiqi Nie [d], Yuechang Wei [e], Huaming Li [a,*], Hui Xu [a,*]

[a] School of Chemistry and Chemical Engineering, Institute of Energy Research, Jiangsu University, Zhenjiang, Jiangsu 212013, PR China
[b] College of Environmental Science and Engineering, Yangzhou University, Yangzhou, Jiangsu 225009, PR China
[c] College of Chemical Engineering, Zhejiang University of Technology, Hangzhou, Zhejiang 310014, PR China
[d] Institute of High Energy Physics, Chinese Academy of Sciences, Beijing 100049, PR China
[e] State Key Laboratory of Heavy Oil Processing, China University of Petroleum, Changping, Beijing 102249, PR China

ARTICLE INFO

ABSTRACT

Adsorption and activation of CO_2, and high carriers transform efficiency are of great significance for improving the CO_2 photoreduction performance. However, electronic structure regulation plays an important role in the dynamical behavior of carriers. In this study, O atoms were successfully introduced into polymeric carbon nitrogen to synthesize an orange O-modified polymeric carbon nitrogen and achieve the rearrangement of electron density distribution, which promotes the adsorption and activation of CO_2 and efficient separation and migration of carriers. DFT calculation demonstrates that the O atoms perform as the dominant active sites and reduce the free energy of determining step. Moreover, the introduction of O atoms broadens the light absorption range by changing the electronic layer structure of polymeric carbon nitrogen. Therefore, the fabricated O-modified polymeric carbon nitrogen exhibits significant performance. Under visible light irradiation, the CO generation efficiency achieved a 10-fold boost. We synthesize theory and experiment to highlight the important role of modulating electronic structure in designing photocatalysts.

1. Introduction

The rapid development of the global economy needs to be supported by a large amount of energy consumption [1]. Especially, the combustion of fossil fuels is inevitably accompanied by the generation of CO_2 [2]. Facing the environmental and energy problems triggered by the serious imbalance between CO_2 excessive emission and consumption, there are a series of negative effects on the development process of industry and the quality of human life [3,4]. Therefore, it is highly urgent to develop an approach that can realize the efficient conversion of CO_2 to high-value-added chemicals [5]. In recent years, photocatalytic CO_2 conversion technology has been favored due to its advantages of environmental friendliness and low cost of driving force [6,7]. The key to restricting the development and practical application of photocatalytic CO_2 conversion technology is the lagging conversion efficiency. Focusing on the process of photocatalytic CO_2 reduction: (1) photogenerated electron-hole pairs are generated by light irradiation on semiconductors; (2) photogenerated electron-hole pairs are separated

and transferred to the surface of the catalyst; and (3) the reduction reaction happens between active species and reactants [8,9]. It is easy to find that carrier behavior plays an important role in catalytic efficiency. Therefore, great efforts have been devoted to designing efficient photocatalysts to achieve efficient CO_2 conversion.

Up to now, a variety of semiconductor materials, such as metal oxide (In_2O_3 [10], Cu_2O [11]), metallic sulfide (ZnS [12], $CuInS_2$ [13]) and metal-organic framework [14,15], etc., have been developed and remarkable achievements have been made in the field of photocatalytic CO_2 reduction, which has paved the way for the future development and practical application of CO_2 reduction technology. In recent years, non-metallic materials have set off a research boom in this field, especially polymeric carbon nitrogen (PCN) [16,17], black phosphorus (BP) [18,19], etc. Among them, PCN is one of the most attractive candidates for CO_2 photoreduction reactions owing to its non-toxicity, earthly abundance and exceptional set of electronic and optical properties [20–22]. However, the main factors limiting its photocatalytic performance are still slow photogenerated carrier transport and high-speed

---

recombination caused by the wide band gap (~2.7 eV) [23,24]. Thus, numerous strategies, such as vacancy construction, element doping and functional group modification, have been applied to narrow the band gap, optimizing the dynamics behavior of photogenerated carriers. For instance, the generation of defect levels can effectively reduce the distance of photogenerated carriers' migration and accelerate charge transfer. Besides, grafting electron-withdrawing groups can effectively construct an electron donor-acceptor (D-A) system to achieve spatial separation of electron-hole pairs [25–27].

Notably, metal atoms doped with PCN can modulate the local electronic structures by acting as electron acceptors [28,29]. The function has been indicated to outstandingly enhance the dynamics properties attributed to it helping with the separation of charge carriers [30]. However, due to the large difference in atomic radius between metal atoms and C/N, it tends to cause the destruction of the basic triazine ring structure and the distortion of the layered structure for PCN [31]. Therefore, the intrinsic properties of PCN will be affected to a certain extent. The oxygen (O) element is not only in the same period as C and N, but also has a similar atomic radius [32,33]. Based on the important role of charge redistribution on electron transfer kinetics, O doping is an ideal candidate for tuning the internal electronic structure of PCN.

Based on the above discussion and previous research by our group, we fabricated a novel orange O-modified polymeric carbon nitrogen (O-PCN) via the strategy of one-step ammonium formate-assisted thermal polymerization and carried out a detailed study of its structure. Additionally, compared with light yellow PCN, the orange O-PCN realizes the broadening of the photoresponse range, which promotes the light-harvesting ability of the material and provides a strong driving force for the occurrence of photocatalytic CO_2 reduction reactions. On the other hand, the successful doping of O into the PCN framework enables electron density redistribution to facilitate efficient carrier transport. The combined studies by XPS, ^{13}C solid-state NMR and XANES revealed the doping sites of O and the structure of O-PCN in detail. The results show that the DFT calculations verified that the higher charge density and electronic structure changes near the O atom promote the adsorption and activation of CO_2 molecules. Therefore, O-PCN manifested significantly improved photocatalytic CO_2 reduction activity under both full-spectrum and visible light illumination. On the basis of the characterization of in-situ FT-IR spectra and calculated free energy diagrams, the possible reaction mechanism and excellent reaction kinetics of O-PCN were successfully demonstrated.

2. Experimental

2.1. The chemicals and materials

Ethanol (99.7%), triethanolamine (TEOA), urea, and ammonium formate were purchased from Sinopharm Chemical Reagent Co. Ltd. All the materials applied for experiments were analytical reagents and were used without any purification.

2.2. Material synthesis

Preparation of PCN: Typically, the PCN was prepared by the technology of thermal polycondensation. In particular, 10 g of urea were fully ground and loaded into a 30 mL crucible. To insulate from the outside world, the tinfoil and lid were used to construct a double repeat before being placed on the muffle furnace. The ramping rate and heating temperature were set to 3 °C/min and 550 °C, respectively. The PCN powder with light yellow was obtained after 70 min of calcination and full grinding.

Preparation of O-PCN: Firstly, 10 g of urea and a certain amount of ammonium formate were mixed by fully grinding and loaded into a 30 mL crucible. Afterward, a series of orange O-PCN with different degrees of orange was obtained by the same calcination step as PCN preparation. These O-PCN were denoted as 0.1 O-PCN, 0.25 O-PCN and 0.4 O-PCN

based on the used ammonium formate amount of 0.1, 0.25 and 0.4 g. (The O-PCN labeled in the picture represents the 0.25 O-PCN with the best activity under the irradiation of 300 W Xe lamp.).

2.3. Characterization

X-ray diffraction (XRD) patterns were measured by an XRD-6100 from Shimadzu corporation with Cu source at 40 kV in the range of 2θ = 10–80°. Scanning electron microscopy (SEM) and Transmission electron microscopy (TEM) images were obtained by JSM-7800 F microscope and a JEM-2100 (HR). XPS spectra were measured on a Thermo Scientific K-Alpha electron spectrometer. Fourier transform infrared (FT-IR) spectra were recorded on a Nicolet Is-50 spectrophotometer. Electron spin resonance (EPR) measurements were recorded on MiniScope MS5000 EPR spectrometer. Photoluminescence (PL) spectra were performed with a QuantaMaster & TimeMaster Spectrofluorometer. Time-resolved photoluminescence decay (TRPD) spectra were performed at FS1000 of Edinburgh Instruments. ^{13}C solid-state NMR spectrum was measured on a Bruker 400 M. Electrochemical impedance spectroscopy (EIS) and time-resolved photocurrent behaviors were performed on the electrochemical workstation in a 3-electrode configuration with the assembled photoelectrodes (photocatalyst on FTO glass) as the working electrode, the Pt slice as the counter electrode and the Ag/AgCl as the reference electrode, and 0.2 M Na_2SO_4 solution was used as electrolyte. For time-resolved photo-current behaviors, a 300 W Xe lamp with a current of 15 A was the light source.

2.4. Photocatalytic CO_2 reduction activity

Photocatalytic CO_2 reduction was tested in a 300 mL closed Pyrex top-irradiation vessel (Labsolar-6A, Beijing Perfectlight). Typically, 10 mg catalyst powder was dispersed in an aqueous solution (16 mL) containing 12 mL H_2O and 4 mL TEOA as hole sacrifice agent. After the air in the reaction system was cleared away, high-purity CO_2 was introduced into the system until the pressure reached 70 kPa and circulated for 60 min to achieve uniform distribution of CO_2 gas. The temperature of photocatalytic CO_2 reduction was set at 10 °C by a cooling water circulation system which can promote the adsorption of CO_2, and a 300 W Xe lamp was employed as the light source. The light intensity of the 300 W Xe lamp is 650 mW/cm^2. The light intensity of the 300 W Xe lamp (λ ≥ 420 nm) is 572 W/cm^2. The light intensity of the 300 W Xe lamp (λ ≥ 520 nm) is 394 W/cm^2. The gas chromatograph (GC2002, KeChuang, Shanghai) equipped with a thermal conductivity detector (TCD) and a hydrogen flame ionized detector (FID) with a capillary column was used to determine the amount of the gas product.

2.5. Density functional theory (DFT) computational methods

The density functional theory (DFT) calculations were performed for structural optimization as implemented in the Vienna ab-initio Simulation Package (VASP). The PBE exchange-correlation functional of the generalized gradient approximation (GGA) was used to describe the exchange correlation energy. The cutoff energy of the all-electron plane-wave was set at 520 eV. In order to avoid the interaction between adjacent layers, the vacuum layer was set at 15 Å. PCN is simulated using a surface model of p (3 × 3) unit cell periodicity composed of 126 atoms. O-PCN is simulated using that a nitrogen atom replaced by an oxygen atom of PCN. The conjugate gradient algorithm was applied for optimization. The convergence threshold was fixed at 1 * 10^{-4} eV in total energy and 0.05 eV/ Å in force on every atom. The free energy change (ΔG) for adsorptions was determined as follows:

$$\Delta G = (E_{total} - E_{slab} - E_{mol}) + \Delta E_{ZPE} - T\Delta S$$

where E_{total} is the total energy for the adsorption state, E_{slab} is the energy of the pure surface, E_{mol} is the energy of the adsorption substrate, ΔE_{ZPE}

is the zero-point energy change and ΔS is the entropy change.

3. Results and discussion

3.1. Preparation and microstructure characterization of catalysts

The synthesis of light yellow PCN and orange O-PCN by simple strategies of high-temperature thermal polycondensation and ammonium formate-assisted high-temperature thermal polymerization of urea is demonstrated in Fig. 1a. The X-ray diffraction (XRD) patterns of the as-prepared catalysts were illustrated in Fig. S1, verifying the successful preparation of PCN. The typical diffraction peaks located at 13.29° and 27.57° correspond to the (100) and (002) crystal planes, representing the in-plane ordered structure stacking and the interlayer structure stacking, respectively [34]. In contrast, significant differences were not observed in the center positions of the diffraction peaks of O-PCN. The similar peak shape at 13.29° reflects that the in-plane long-range order structure is unbroken [35]. However, the significantly broader peak at 27.57° reveals a weakening of the interlayer interactions [36]. To further obtain information on the microstructure of PCN and O-PCN, the Fourier transform infrared (FTIR) spectra were measured. As shown in Fig. S2, the characteristic peaks of PCN and O-PCN are assigned to the bending mode of heptazine rings, the stretching vibration of the C-N heterocyclic ring and the tensile vibration of the N-H group are distributed at 810 cm^{-1}, 1100–1800 cm^{-1} and 3000–3300 cm^{-1}, respectively [37]. This performance indicates that the basic frame structure is not damaged with the introduction of ammonium formate in the precursor. Obviously, the reduced intensity of the peaks located at 1100–1800 cm^{-1} of O-PCN demonstrates a change in aromatic C=N or C-N species [38]. The prominent peak around 3400 cm^{-1} originals for more abundant OH species on the surface of O-PCN, which lays a good foundation for the improvement of hydrophilic performance [36]. This result needs to be further determined by static water contact angle measurements. As shown in Fig. S3, O-PCN exhibits a smaller contact angle of 27.73° compared with that of PCN (37.11°), illustrating higher surface hydrophilicity. Based on the above results, it can be inferred that the heterocyclic ring elements may be substituted by doping elements.

From the results of element analysis (EA) shown in Fig. 1b, it is found that the content of the C element remained stable, while the percentage of N element continued to decrease with the increase of glycolic acid content. Notably, the percentage of the O element increased gradually, implying the successful doping of the O may be at the N site. The surface chemical state of catalysts was further investigated by X-ray photoelectron spectroscopy (XPS). XPS survey spectra illustrate that PCN and O-PCN consist of C, N and O elements (Fig. S4). Compared with the O 1 s XPS spectra (Fig. 1c) of PCN and O-PCN, similar major peaks centered at near 531.6 and 532.9 eV are attributed to the N-C-O and C-O bonds, respectively [38]. The significant increase in the proportion of
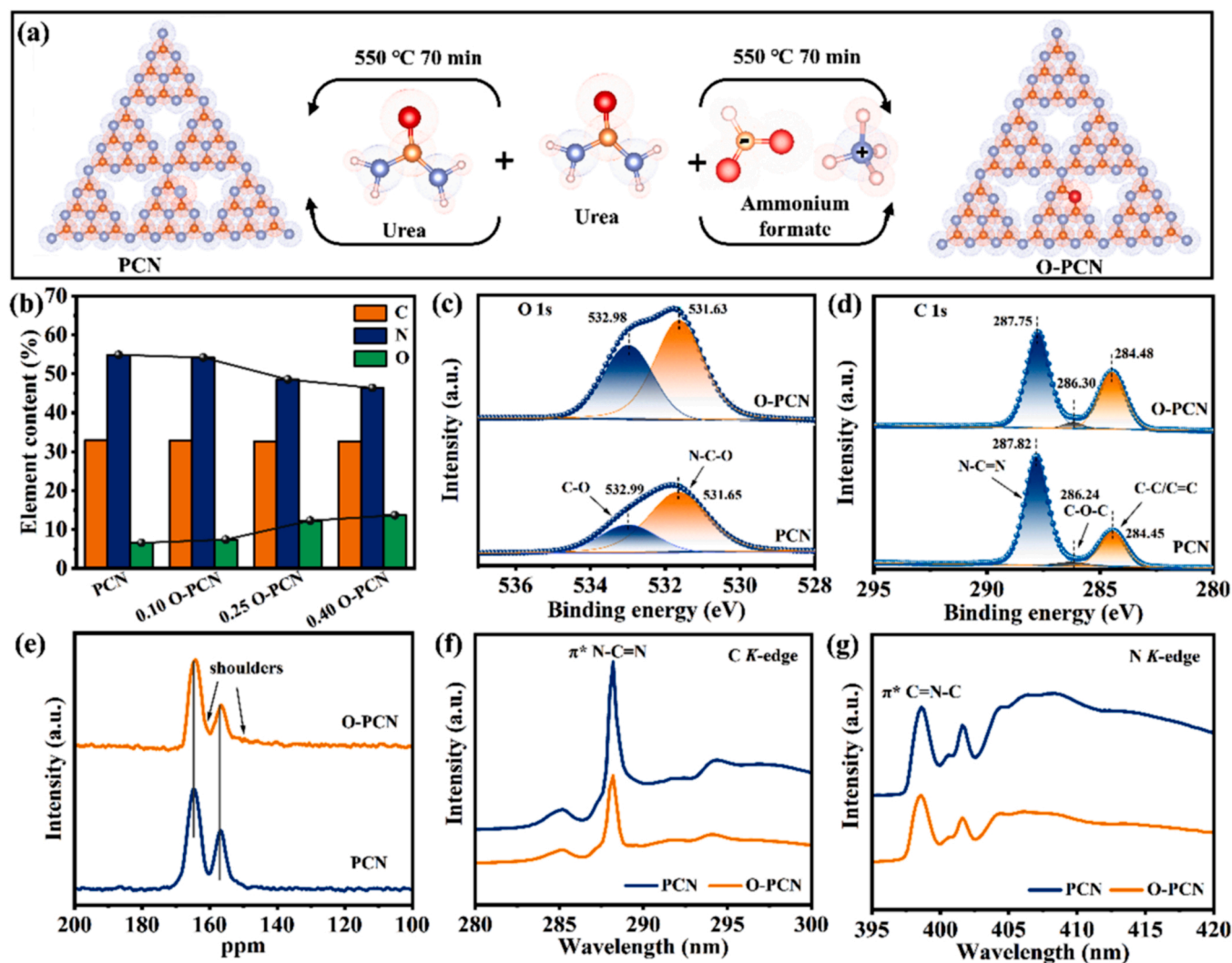

Fig. 1. (a) Schematic illustration for preparing PCN and O-PCN. (b) Element composition of samples. O 1 s(c), C 1 s (d) in XPS, (e) ^{13}C solid-state NMR spectra, XANES curves of C K-edge (f) and N K-edge (g) of PCN and O-PCN.

characteristic peak areas assigned to C-O bonds further implies that more O species are introduced into O-PCN forming bonds with C. Simultaneously, the 286.3 eV signal (C-O-C) of O-PCN in C 1 s XPS spectra (Fig. 1d) was evidently prominent compared with that of PCN, which provides additional assistance for the successful doping of the O element [39]. The binding energy of N-C≡N and C≡N-C in O-PCN is slightly lower than that of PCN (Fig. S5) [40]. The solid-state ^{13}C NMR (CP-MAS) tests were also investigated to reveal the chemical structure of O-PCN. As depicted in Fig. 1e, PCN exhibits two characteristic peaks at 156.7 and 164.7 ppm, which correspond to the C atom in CN_2-NH_X and CN_3 groups, respectively. In particular, the intensity of the peak attributable to C of CN_3 decreased significantly in O-PCN, which may be attributed to N atoms in tri-s-triazine being replaced by O. Moreover, the appearance of two extra shoulder peaks suggests that the generation of new C species is based on the environmental changes near C atoms caused by the substitution of O for part of N [41]. The above results reveal that the doping site is N of O-doping.

The composition of catalysts is closely related to photocatalytic performance. Thus, it is crucial to accurately reveal the chemical structure of O-PCN since the N element exists in many forms in PCN. The K-edge X-ray absorption near-edge structure (XANES) can provide firm evidence about the simultaneous doping site of O atoms. As illustrated in Fig. 1f, the C K-edge XANES spectra of PCN and O-PCN both display a classical peak of $\pi *$ $_{N-C-N}$ at 288.2 eV originating from the C 1 s orbital transition [35]. The signal intensity is significantly attenuated for O-PCN in comparison to PCN, highlighting that part of the N≡C-N groups is breaking with the introduction of O atoms in the tri-s-triazine motifs. The typical 2p $\pi *$ response signal appears as two characteristic peaks corresponding to $\pi *$ $_{C-N-C}$ (398.6 eV) and $\pi *$ $_{N-(C)3}$ (401.6 eV) in the N K-edge XANES spectra shown in Fig. 1g [42]. In comparison, although the intensity of two 2p $\pi *$ peaks of O-PCN has been attenuated to different degrees, the reduction of the characteristic peaks attributed to C≡N-C is more prominent, strongly implying that the main doping site of O is N in the tri-s-triazine motifs. Besides, the density functional theory (DFT) was performed to investigate the formation energies (E_f) of O substitution at two types of N sites. As observed in Fig. S6, the lowest

E_f is attributed to Model 2, indicating that O atoms are more inclined to replace N1, which is in perfect agreement with the results of the above experimental characterizations. In order to demonstrate that ammonium formate plays an important role in the urea polycondensation process, control experiments for O-PCN preparation were carried out as shown in Fig. S7. The ammonium formate was added after urea polycondensation and calcined for a second time. Interestingly, the product color remains the same light yellow as PCN confirmed that ammonium formate played a role in introducing oxygen species into the system during the urea polycondensation process. Besides, the results of thermogravimetric (TG) (Fig. S8) show that the introduction of ammonium formate has no obvious effect on the thermal condensation process.

The microstructure and morphology of PCN and O-PCN were investigated via scanning electron microscopy (SEM) and transmission electron microscopy (TEM). As shown in Fig. S9, PCN exhibited massively coiled and packed irregular nanosheets. In detail, TEM images revealed that PCN was composed of dense and irregular ultrathin nanosheets (Fig. S10). Although the orange O-PCN still displays a nanosheet structure, the rich pore structure is distributed on the surface of the nanosheets (Fig. 2a and b), which may benefit from the generation of a high concentration of NH_3 during the calcination process. The nitrogen adsorption-desorption isotherm is observed in Fig. S11, which presents a typical type IV isotherm of PCN and O-PCN. Based on abundant pores, O-PCN possesses a larger specific surface area (52.75 m^2/g) than that of PCN (44.75 m^2/g). Atom force microscopy (AFM) images reveal the thickness of PCN and O-PCN is 3–4 nm (Fig. 2c and d, Fig. S12). Moreover, large holes can still be clearly observed. Based on the above analysis, the unique pore structure not only enhances the specific surface area of PCN but also provides a broader platform for the exposure of active sites. More attractively, the existence of holes provides more shortcuts for the transfer of carriers and makes the interlayer transport of carriers easier. In addition, the mapping images (Fig. 2e-h) demonstrated that C, N, and O are evenly distributed in O-PCN.
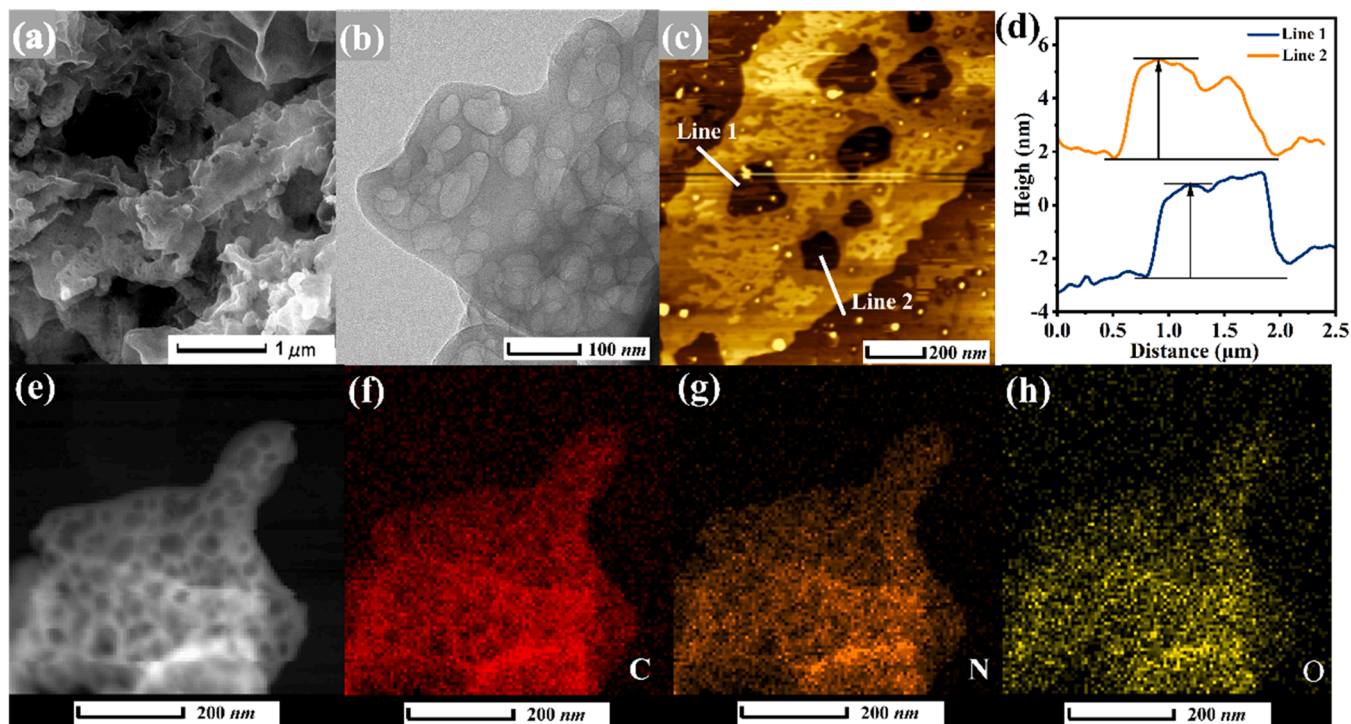
Fig. 2. (a) SEM image, (b) TEM image, (c) AFM image, and (d) height profile of O-PCN. (e) TEM image and corresponding C (f), N (g), and O (h) elements mapping images of O-PCN.

3.2. The evaluation of photocatalytic performance

The photocatalytic performance is evaluated by CO_2 reduction under a 300 W Xe lamp with triethanolamine (TEOA) as a hole sacrifice agent. A gas chromatography (GC) online system is used to detect possible gas products. As the comparison of product evolution rates over a series of photocatalysts presented in Fig. 3a, PCN indicates low CO_2 reduction catalytic activity with CO, CH_4 and H_2 generation rates of 34.50 μmol g^{-1} h^{-1}, 8.17 μmol g^{-1} h^{-1} and 5.09 μmol g^{-1} h^{-1}. However, these O-PCN with different ammonium formate additions showed significantly improved catalytic activity, especially the generation efficiency of CO. At the same time, as the amount of ammonium formate increased from 0.1 to 0.4 g, the inhibitory effect of the hydrogen generation reaction was more significant, and even no hydrogen was detected for the catalyst of 0.40 O-PCN. Notably, the highest CO generation rate of 144.75 μmol g^{-1} h^{-1} attributed to 0.25 O-PCN is approximately four times that of PCN. However, with the addition of more ammonium formate, the catalyst performance gradually decreased. When the addition amount was increased to 0.4 g, the obtained material hardly exhibited the photocatalytic CO_2 reduction ability, showing more disappointing performance than PCN. Furthermore, when the filter ($λ ≥ 420$ nm) is mounted on a 300 W Xe lamp, O-PCN still exhibits outstanding CO generation efficiency (15.97 μmol g^{-1} h^{-1}) that is approximately ten times that of pristine PCN (Fig. 3b). The reaction can be carried out under $λ ≥ 520$ nm illumination and the CO yield of O-PCN reaches above 6.22 μmol g^{-1} h^{-1}. The reasons for the above phenomena will be discussed in detail in the next section. As seen in Table S1, the designed O-PCN catalysts exhibit competitive CO_2 reduction performance among a series of PCN-based photocatalysts.

In order to verify the photocatalytic properties of the best catalyst, the CO_2 reduction experiment was run under dark conditions (Fig. S13). The characteristic peaks of any product are captured by GC, revealing that sunlight is the strong driver of the reaction. When no catalyst was added to the reaction system, almost no photocatalytic CO_2 conversion process was observed, denoting that photocatalysts play a vital role in the photocatalytic CO_2 reduction reaction. In addition, when the CO_2 was replaced by Ar in the catalytic system, only trace amounts of H_2 were detected in the product, revealing that the carbon source in the carbon-containing product is likely to come from CO_2. A more convincing isotopic labeling experiment of $^{13}CO_2$ was performed to further verify the carbon source of the reaction. In Fig. 3c, the signal of $m/z = 17.0$ and $m/z = 29.0$ corresponds to $^{13}CH_4$ and ^{13}CO in the mass spectra, confirming that CO and CH_4 indeed originate from CO_2 rather than the decomposition of carbon residues on the catalyst. Additionally, only a small amount of CO was detected in the activity test experiments where TEOA was removed. Satisfactorily, O-PCN showed a relatively stable product formation rate during the 25 h with 5 cycle performance tests (Fig. 3d). Simultaneously, after cyclic testing, the XRD peaks (Fig. S14) and SEM images (Fig. S15) of the O-PCN did not change significantly.

3.3. Explore the cause of increased photocatalytic activity

Based on the significant improvement of the photocatalytic CO_2 reduction performance of the O-PCN, various characterizations were carried out to clearly reveal and explore the effects of O-doping on its light absorption properties, energy band structure, photoelectric performance, and adsorption and activation of CO_2. In essence, the UV–vis diffuse reflectance spectrum (DRS) of catalysts is illustrated in Fig. 4a. Based on the $π$-$π$* electron transition induced by C-N heterocycles containing $π$-conjugation, the light yellow PCN exhibits obvious light absorption properties at 200–450 nm [35]. It is worth noting that the orange O-PCN broadens the photoresponse range based on the intrinsic absorption of PCN. Interestingly, there is an obvious absorption peak bulge phenomenon in the back at 450–600 nm, which is attributed to the contribution of unpaired electrons from C-O groups to the
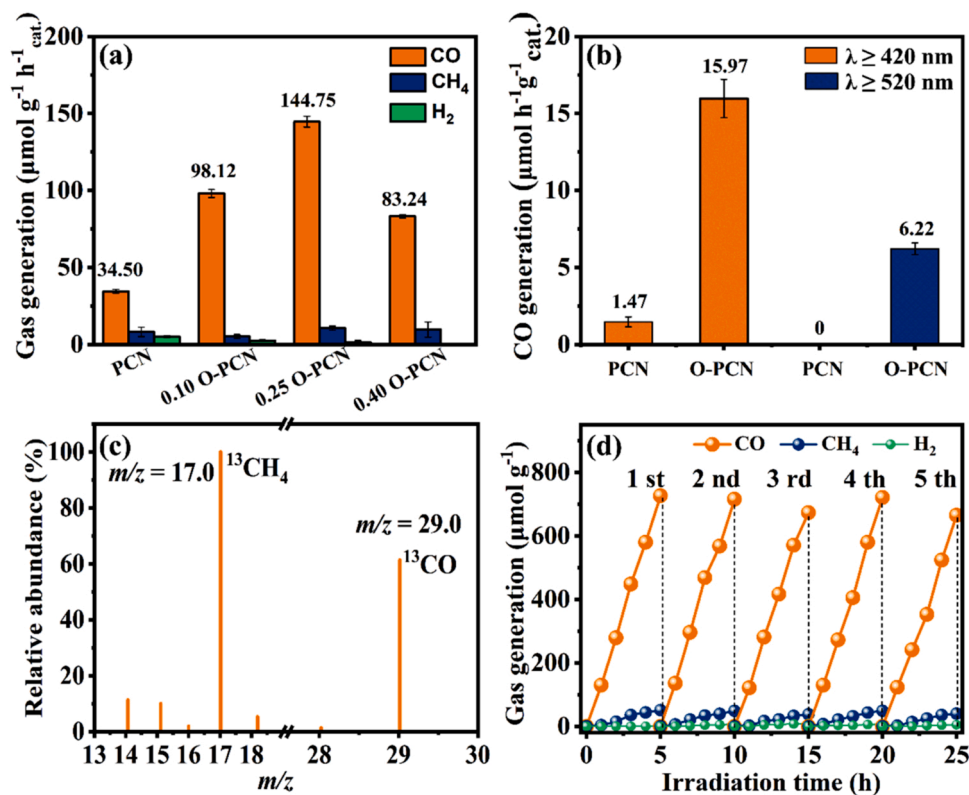
Fig. 3. (a) Time courses of photocatalytic product evolutions samples. (b) Time courses of photocatalytic product evolutions over PCN and O-PCN under a 300 W Xe lamp ($λ ≥ 420$ nm and $λ ≥ 520$ nm). (c) Mass spectra of ^{13}CO ($m/z = 29$) and $^{13}CH_4$ ($m/z = 17$) produced over O-PCN in photocatalytic reduction of $^{13}CO_2$. (d) Stability test of O-PCN for photocatalytic CO_2 reduction.

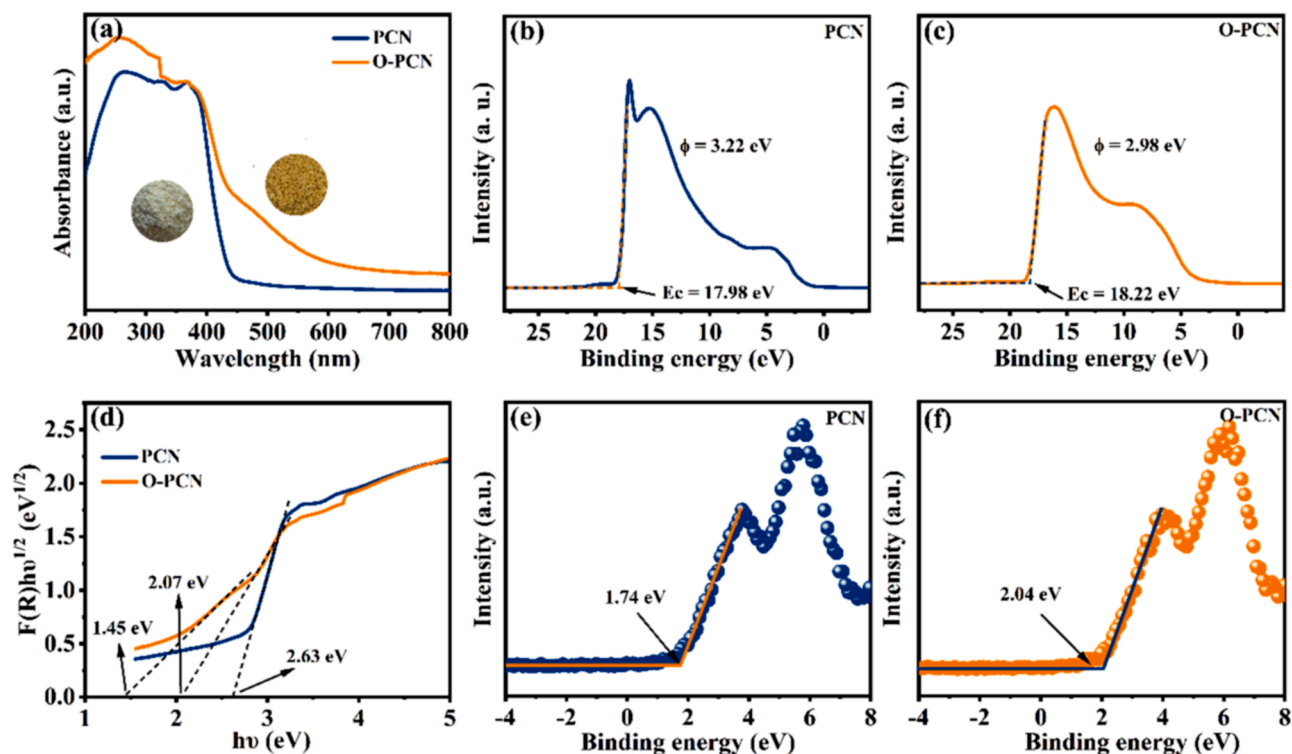**Fig. 4.** (a) UV–vis DRS and UPS of PCN (b) and PCN (c). (d) Tauc plots and XPS-VB spectra of PCN (e) and O-PCN (f).

n-π * electron transition. In addition, the redshift of the absorption edge is inseparable from the color change of the catalyst. According to the corresponding Tauc plots (Fig. 4b), the bandgaps of PCN and O-PCN are deduced as 2.63 and 2.07 eV. The calculated work functions of PCN and O-PCN are 3.22 and 2.98 eV from the result of ultraviolet photoelectron spectroscopy (UPS) combined with the equation: $\Phi = 21.22 - E_C$ (E_C: the cut-off binding energy in Fig. 4c and d) [43]. The XPS valence band (XPS-VB) spectra are shown in Fig. 4e and f, markedly indicating the E_{CB} of PCN and O-PCN are -2.33 and -2.95 V relative to the vacuum level. According to the equation: E(RHE) = –E(Vacuum) – 4.44 eV [44], the
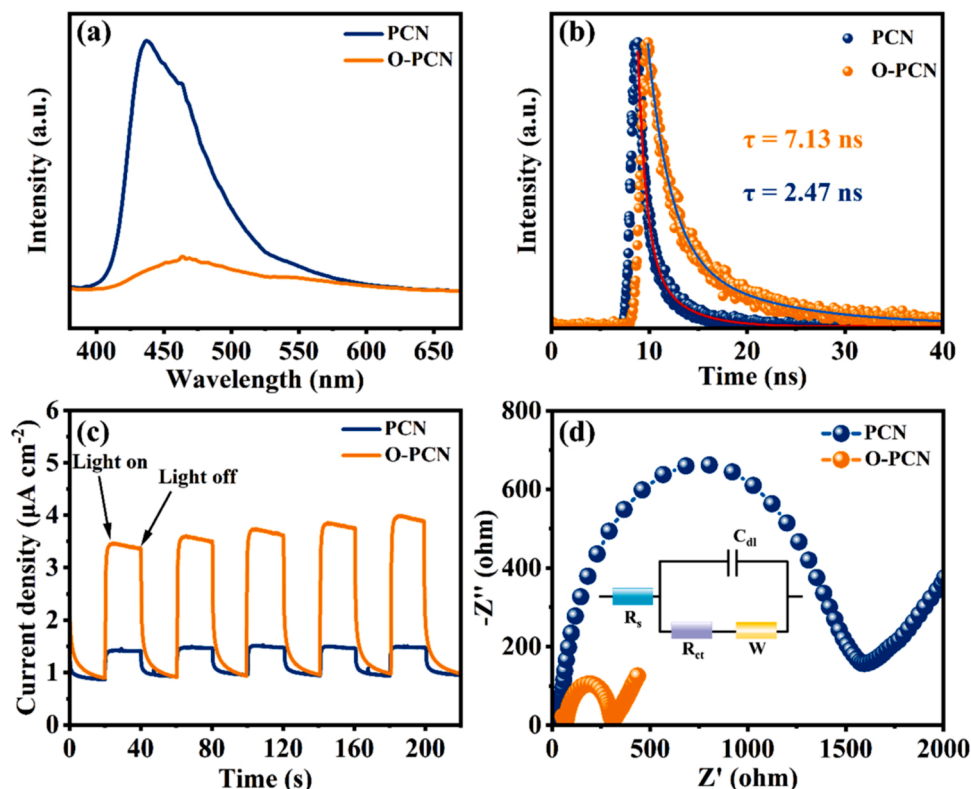

Fig. 5. (a) PL spectra, (b) TRPL spectra, (c) time-dependent photocurrent, (d) EIS measurement of PCN and O-PCN.

E_{CB} of PCN and O-PCN relative to the normal hydrogen electrode (RHE) are − 2.11 and − 1.49 V. Therefore, calculated by the formula RHE = NHE + 0.0591 *pH, the E_{CB} (vs NHE) is estimated to be − 2.52 and − 1.90 V. Combining the above results and considering the formula E_{VB} = E_{CB} + Eg [45], the E_{VB} of PCN and O-PCN is calculated to be about 0.11 and 0.17 V. Thus, the trivial band structure diagram is integrated with Fig. S16. It indicates that the introduction of O species expands the photoresponse range of the material and provides the possibility for the efficient utilization of sunlight. Besides, it is proved that the energy band of PCN can be effectively tuned to be narrower through the strategy of oxygen doping. Moreover, the thermodynamic demands of the photocatalytic CO_2 reduction reaction are not hindered due to the still negative potential of CO_2 reduction to CO and CH_4.

Further, the dynamic behavior of photogenerated electrons of O-PCN is further evaluated by photoluminescence (PL) spectra, time-resolved photoluminescence (TRPL) spectra and photo-electrochemistry tests. To be specific, as described in Fig. 5a for the PL spectra, the distinctly prominent PL response reveals the carriers of PCN are easy recombination. However, with the introduction of more oxygen elements into the triazine ring, the better charge separation efficiency of O-PCN is reflected in a smaller PL intensity compared to that of PCN. Besides, in order to explore the charge transfer efficiency, TRPL spectra decay spectroscopy was used to further investigate the average exciton lifetime. Through the result of the biexponential decay function in Fig. 5b, the carrier lifetime of O-PCN (7.13 ns) is clearly prolonged to about three times that of pristine PCN (2.47 ns), suggesting the enhanced charge transfer efficiency and the ability to inhibit the photogenerated carrier recombination of O-PCN [46,47]. From the transient photocurrent spectra (Fig. 5c and Fig. S17), when the light is on, O-PCN presents a higher photocurrent density, indicating an excellent effect on the separation and diffusion of photogenerated electron-hole pairs. The smaller arc radius in the Nyquist plot electrochemical impedance spectroscopy (EIS) in Fig. 5d further verifies the excellent charge separation efficiency of O-PCN [48]. All the above characterization together shows that the introduction of the O element effectively improves the optoelectronic properties of the pristine PCN by adjusting the internal electronic structure of the material to promote the separation and transfer of photogenerated carriers, which is beneficial to the efficient improvement of the photocatalytic CO_2 reduction performance.

Meanwhile, DFT calculation was carried out to investigate the effect of O's introduction on the electronic structure. First of all, we constructed the models of PCN and O-PCN triazine structural units to calculate their planar electrostatic formula and Bader charge. In Fig. 6a and b, the calculated electrostatic potential (ESP) distribution of O-PCN demonstrates a larger electron-rich region corresponding to the red region located around the oxygen element. Compared to the same position in PCN, the internal structure of O-PCN is more conducive to efficient electron transport thanks to the more substantial electron concentrations of both the introduced oxygen sites and the surrounding nitrogen sites. Furthermore, in order to verify the specific value of charge distribution, the Bader charge was summarized and compared in Fig. 6c and d. The O atom accumulates an electron density of 7.023 eV, which is obviously higher than that of N1 (6.137 eV) in PCN. The reason for this phenomenon can be inferred to be the stronger electronegativity of O. Notably, the electron density of N2, N3 and N4 also increased significantly. Meanwhile, the electron concentration decay of adjacent C atoms after substituting some nitrogen atoms with O atoms further verified the stronger charge transfer behavior of O-PCN. Moreover, electron paramagnetic resonance (EPR) patterns (Fig. 7a) show that a stronger EPR signal is attributed to O-PCN, indicating more accumulation of unpaired electrons on its surface. Combining the above theoretical and experimental characterization analysis, the introduction of oxygen leads to the redistribution of charges in the system, which promotes efficient electron transport and is beneficial to the absorption and activation of CO_2 molecules. To obtain convincing evidence, Fig. 6e and f present more negative CO_2 adsorption energies (E_{ads}) of O-PCN indicating its stronger adsorption capacity for CO_2. The CO_2 adsorption isotherms were also tested to further investigate the adsorption capacity of the catalyst for CO_2. The result (Fig. 7b) is consistent with the calculated E_{ads} for the CO_2 trend. Besides, the calculated differential charge density reveals more charge transfer between the catalyst and CO_2 molecules after O atoms are introduced into PCN. The planar-averaged charge density (Fig. 6 g and h) visualizes the above results, indicating that the stronger interaction between O-PCN and CO_2 lays the foundation for further CO_2
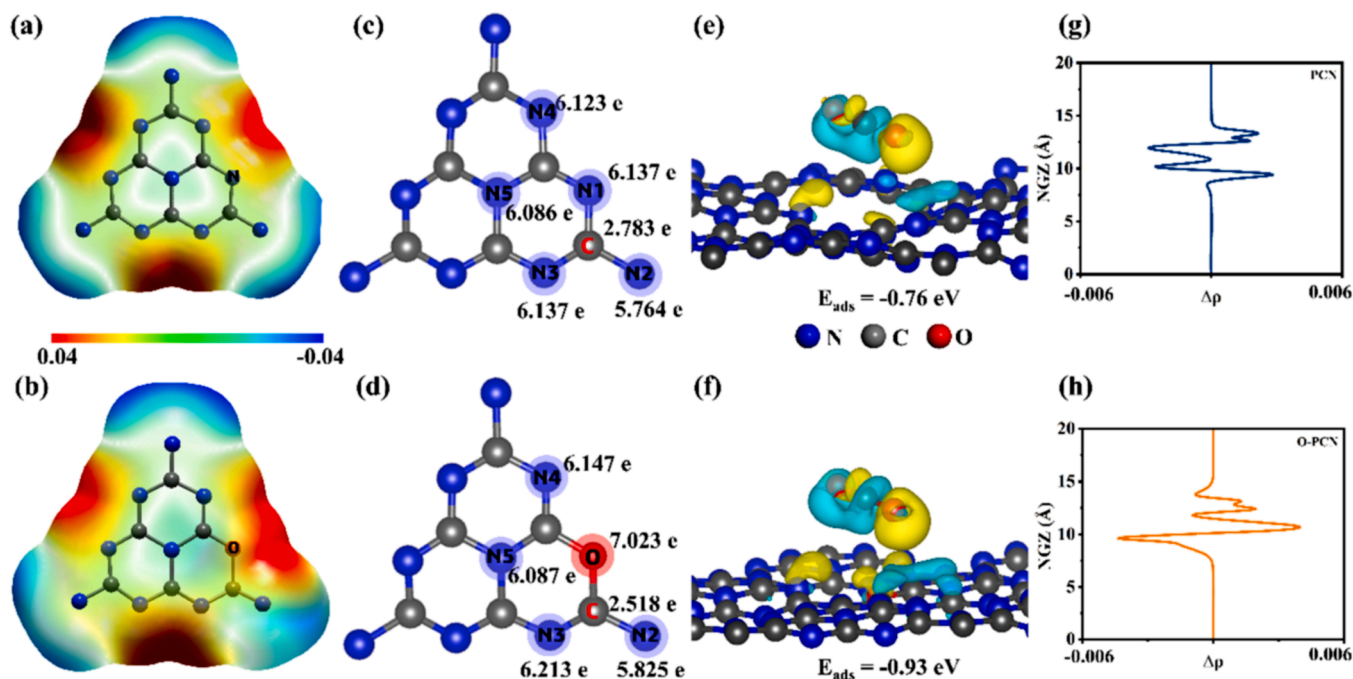

Fig. 6. (a-b) ESP distribution, (c-d) calculated Bader charge, (e-f) charge difference density distribution and (g-h) plane-averaged charge density difference of PCN and O-PCN.
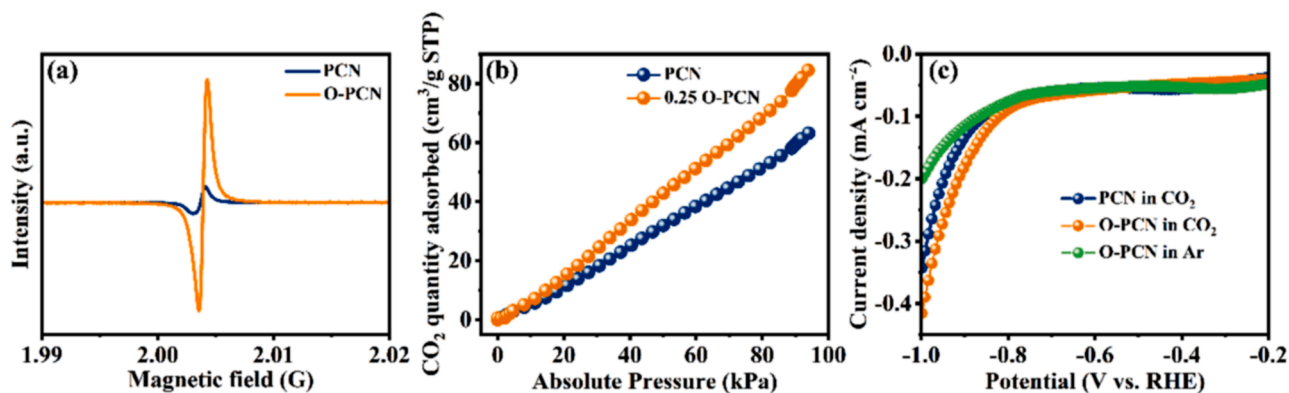
Fig. 7. (a) EPR patterns, (b) CO_2 adsorption isotherms and (c) LSV of PCN and O-PCN.

activation. In addition, linear sweep voltammetry (LSV) curves of O-PCN (Fig. 7c) display a more positive initial potential in the CO_2 atmosphere than that in Ar, verifying that it can activate CO_2 molecules. Moreover, the LSV of PCN in CO_2 atmosphere exhibits lower current density and a more negative initial potential, further indicating the more dominant ability of O-PCN to activate CO_2 [49].

3.4. The CO_2 photoreduction pathway and mechanism of O-PCN

The *in-situ* Fourier transform infrared (*in-situ* FTIR) spectroscopy with solar illumination time from 0 to 30 min is illustrated in Fig. 8a and b for identifying the possible reaction pathways of CO generation. It is

worth noting that PCN and O-PCN diffracted the following series of characteristic peaks at the same positions. The peaks at ~1654.5, ~1348.3 and ~1289.0 cm^{-1} were attributed to H_2O, a reaction intermediate of bidentate carbonate (b-CO_3^{2-}) and monodentate carbonate (m-CO_3^{2-}), respectively. The HCO_3 species were detected to be located at ~1396.5 and ~1214.0 cm^{-1}. It is noteworthy that the characteristic peaks observed at ~1616.4 and ~1450.1 cm^{-1} originate from the key intermediate of the reaction CO_2^- [50]. By comparing the *in-situ* FTIR spectra of the two kinds of catalysts, the following findings can be obtained: (1) the intermediate species remain the same, indicating the same reaction path; (2) as the reaction time increases, the characteristic peaks of each intermediate become more and more obvious, but the
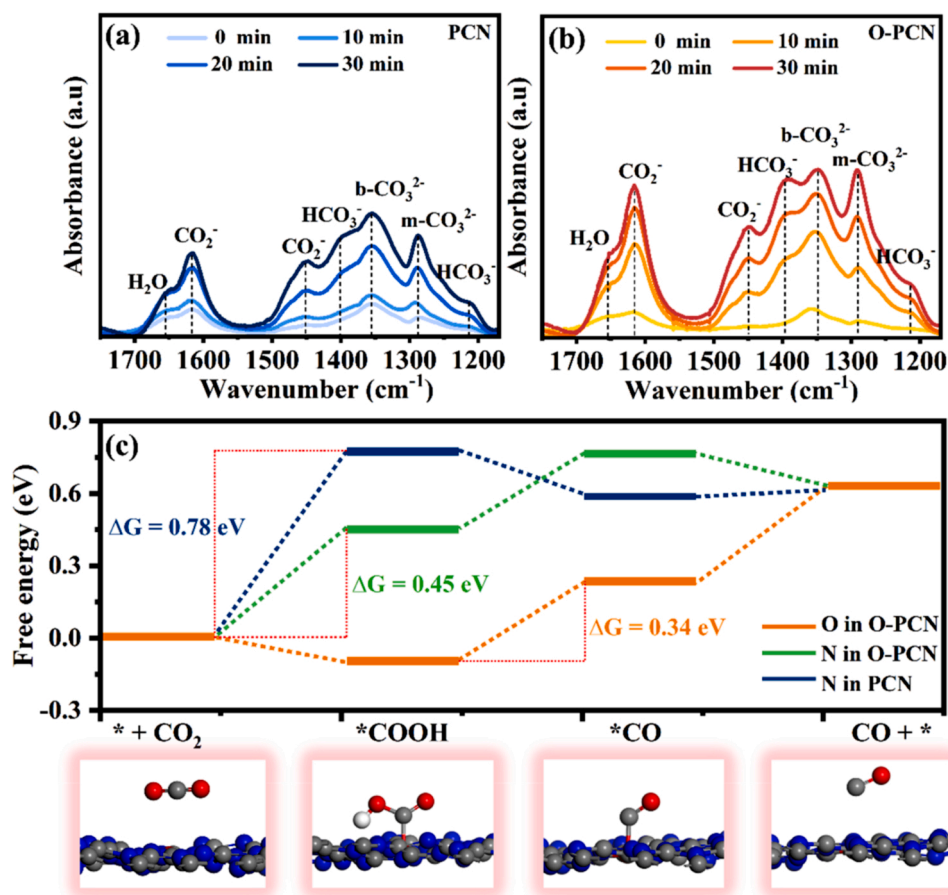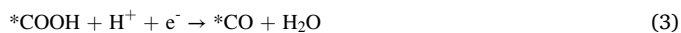

Fig. 8. The *in-situ* FTIR spectroscopy of PCN (a) and O-PCN. (c) The free energy diagram of photocatalytic CO_2 reduction and intermediate adsorption model of O-PCN.

increase of O-PCN is greater to verify its efficient reaction rate. Combining the above experimental results, possible paths of CO generation can be deduced as follows [51]:

$$* + CO_2 \rightarrow {}^*CO_2 \tag{1}$$

$$^*CO_2 + H^+ + e^- \rightarrow {}^*COOH \tag{2}$$

$$^*COOH + H^+ + e^- \rightarrow {}^*CO + H_2O \tag{3}$$

$$^*CO \rightarrow CO\uparrow + * \tag{4}$$

Further, DFT calculations were applied to the investigation of CO_2 reduction reaction free energy to reveal the effect of O species on the CO generation process. For the purpose of the above properties, we selected O and equivalent N in O-PCN models as active sites for theoretical simulations, respectively. In addition. The equivalent N in PCN was used as a control group. The free energy diagram of photocatalytic CO_2 reduction is depicted in Fig. 8c. When the reduction reactions were carried out with N atoms as the reaction site, the rate-limiting step was the formation of *COOH. However, with the successful doping of O elements, the free energy of the rate-limiting step was significantly reduced (0.45 eV), which indicated that the O doping could effectively enhance the activity of the surrounding N sites. Remarkably, when the reaction proceeds at the O site of PCN, the rate-limiting step shifts to the formation of *CO and shows the lowest energy barrier of 0.34 eV. The results of free energy diagrams perfectly fit with the calculated Bader charge and further illustrate that the introduction of O can not only lower the reaction energy barrier as the dominant active site but also effectively enhance the activation and reduction of CO_2 by the surrounding primitive N active sites.

4. Conclusion

To conclude, a series of outstanding broad-spectrum response O-PCN photocatalysts were successfully fabricated and developed for photocatalytic CO_2 reduction to produce carbon-based fuels. Compared to the performance of light yellow PCN, orange O-PCN exhibits praiseworthy photocatalytic CO_2 reduction performance and excellent stability, with a CO evolution rate of $144.75 \ \mu mol \ g^{-1} \ h^{-1}$, which is about 3 times higher than that of PCN under 300 W Xe light irradiation. More importantly, under visible light irradiation ($\lambda \geq 420$ nm), O-PCN also shows improved performance for the reduction of CO_2 to CO, which delivers a CO evolution rate of $15.97 \ \mu mol \ g^{-1} \ h^{-1}$. Even with the addition of a cut-off filter $\lambda \geq 520$ nm, O-PCN can still promote the CO_2 conversion to CO. The unique morphology and atomic arrangement of O-PCN efficiently promote the adsorption and activation of CO_2. DFT calculation revealed that O doping not only provides additional advantageous active sites but also improves the activity of surrounding N sites by modulating charge distribution and band structure. The multiscale microstructural and electronic structure regulations provide more opportunities for the design of photocatalysts in CO_2 reduction reactions.

CRediT authorship contribution statement

H. Xu and J.M. Yang : Conceptualization, Methodology, Data curation. **J.M. Yang**: Data curation, Writing – original draft. **Y.B. She and Y.C. Wei** : Validation, Formal analysis. **K.Q. Nie and J.J. Deng** : Validation. **X.W. Zhu**: Investigation, Writing – review & editing. **L.Q. Jing and W. Zhang** : Visualization, Investigation. **H.M. Li and H. Xu** : Supervision, Project administration, Funding acquisition. All authors contributed to the discussion and preparation of the manuscript.

Declaration of Competing Interest

The authors declare that they have no known competing financial interests or personal relationships that could have appeared to influence the work reported in this paper.

Data availability

No data was used for the research described in the article.

Appendix A. Supporting information

Supplementary data associated with this article can be found in the online version at doi:10.1016/j.apcatb.2022.122005.

References

[1] Y. Zhang, D. Yao, B. Xia, M. Jaroniec, J. Ran, S.Z. Qiao, Photocatalytic CO_2 reduction: identification and elimination of false-positive results, ACS Energy Lett. 7 (2022) 1611–1617.

[2] T. Ahmad, S. Liu, M. Sajid, K. Li, M. Ali, L. Liu, W. Chen, Electrochemical CO_2 reduction to C2+ products using Cu-based electrocatalysts: a review, Nano Res. Energy 1 (2022) 9120021.

[3] S.C. Peter, Reduction of CO_2 to chemicals and fuels: a solution to global warming and energy crisis, ACS Energy Lett. 3 (2018) 1557–1561.

[4] J. Yang, H. Du, Q. Yu, W. Zhang, Y. Zhang, J. Ge, H. Li, J. Liu, H. Li, H. Xu, Porous silver microrods by plasma vulcanization activation for enhanced electrocatalytic carbon dioxide reduction, J. Colloid Interface Sci. 606 (2022) 793–799.

[5] S. Rodriguez-Jimenez, H. Song, E. Lam, D. Wright, A. Pannwitz, S.A. Bonke, J.J. Baumberg, S. Bonnet, L. Hammarstrom, E. Reisner, Self-assembled liposomes enhance electron transfer for efficient photocatalytic CO_2 reduction, J. Am. Chem. Soc. 144 (2022) 9399–9412.

[6] G. Yang, S. Li, N. Li, P. Zhang, C. Su, L. Gong, B. Chen, C. Qu, D. Qi, T. Wang, J. Jiang, Enhanced photocatalytic CO_2 reduction through hydrophobic microenvironment and binuclear cobalt synergistic effect in metallogels, Angew. Chem. Int. Ed. (2022), e202205585.

[7] S. Barman, A. Singh, F.A. Rahimi, T.K. Maji, Metal-free catalysis: a redox-active donor-acceptor conjugated microporous polymer for selective visible-light-driven CO_2 reduction to CH_4, J. Am. Chem. Soc. 143 (2021) 16284–16292.

[8] J. Yang, X. Zhu, Q. Yu, G. Zhou, Q. Li, C. Wang, Y. Hua, Y. She, H. Xu, H. Li, Plasma-induced defect engineering: boosted the reverse water gas shift reaction performance with electron trap, J. Colloid Interface Sci. 580 (2020) 814–821.

[9] G. Liu, B. Wang, X. Zhu, P. Ding, J. Zhao, H. Li, Z. Chen, W. Zhu, J. Xia, Edge-site-rich ordered macroporous BiOCl triggers CO activation for efficient CO_2 photoreduction, Small 18 (2022) 2105228.

[10] J. Yang, X. Zhu, Q. Yu, M. He, W. Zhang, Z. Mo, J. Yuan, Y. She, H. Xu, H. Li, Multidimensional In_2O_3/In_2S_3 heterojunction with lattice distortion for CO_2 photoconversion, Chin. J. Catal. 43 (2022) 1286–1294.

[11] Z. Tang, W. He, Y. Wang, Y. Wei, X. Yu, J. Xiong, X. Wang, X. Zhang, Z. Zhao, J. Liu, Ternary heterojunction in rGO-coated Ag/Cu_2O catalysts for boosting selective photocatalytic CO_2 reduction into CH_4, Appl. Catal. B Environ. 311 (2022), 121371.

[12] A. Sabbah, I. Shown, M. Qorbani, F.Y. Fu, T.Y. Lin, H.L. Wu, P.W. Chung, C.I. Wu, S.R.M. Santiago, J.L. Shen, K.H. Chen, L.C. Chen, Boosting photocatalytic CO_2 reduction in a ZnS/$ZnIn_2S_4$ heterostructure through strain-induced direct Z-scheme and a mechanistic study of molecular CO_2 interaction thereon, Nano Energy 93 (2022), 106809.

[13] J. Yang, X. Zhu, Z. Mo, J. Yi, J. Yan, J. Deng, Y. Xu, Y. She, J. Qian, H. Xu, H. Li, A multidimensional In_2S_3-$CuInS_2$ heterostructure for photocatalytic carbon dioxide reduction, Inorg. Chem. Front. 5 (2018) 3163–3169.

[14] X. Zhao, M. Xu, X. Song, X. Liu, W. Zhou, H. Wang, P. Huo, Tailored linker defects in UiO-67 with high ligand-to-metal charge transfer toward efficient photoreduction of CO_2, Inorg. Chem. 61 (2022) 1765–1777.

[15] A.A. Zhang, D. Si, H. Huang, L. Xie, Z.B. Fang, T.F. Liu, R. Cao, Partial metalation of porphyrin moieties in hydrogen-bonded organic frameworks provides enhanced CO_2 photoreduction activity, Angew. Chem. Int. Ed. 61 (2022) e202203955.

[16] X. Shi, Y. Huang, Y. Bo, D. Duan, Z. Wang, J. Cao, G. Zhu, W. Ho, L. Wang, T. Huang, Y. Xiong, Highly selective photocatalytic CO_2 methanation with water

vapor on single-atom platinum-decorated defective carbon nitride, Angew. Chem. Int. Ed. 134 (2022) e202203063.

[17] X. Chen, Y. Chen, X. Liu, Q. Wang, L. Li, L. Du, G. Tian, Boosted charge transfer and photocatalytic CO_2 reduction over sulfur-doped C_3N_4 porous nanosheets with embedded SnS_2-SnO_2 nanojunctions, Sci. China Mater. 65 (2022) 400–412.

[18] X. Zhu, G. Zhou, J. Yi, P. Ding, J. Yang, K. Zhong, Y. Song, Y. Hua, X. Zhu, J. Yuan, Y. She, H. Li, H. Xu, Accelerated photoreduction of CO_2 to CO over a stable heterostructure with a seamless interface, ACS Appl. Mater. Interfaces 13 (2021) 39523–39532.

[19] X. Zhu, S. Huang, Q. Yu, Y. she, J. Yang, G. Zhou, Q. Li, X. She, J. Deng, H. Li, H. Xu, In-situ hydroxyl modification of monolayer black phosphorus for stable photocatalytic carbon dioxide conversion, Appl. Catal. B Environ. 269 (2020), 118760.

[20] C. Cometto, R. Kuriki, L. Chen, K. Maeda, T.C. Lau, O. Ishitani, M. Robert, A carbon nitride/Fe quaterpyridine catalytic system for photostimulated CO_2-to-CO conversion with visible light, J. Am. Chem. Soc. 140 (2018) 7437–7440.

[21] J. Fu, B. Zhu, C. Jiang, B. Cheng, W. You, J. Yu, Hierarchical porous O-doped g-C_3N_4 with enhanced photocatalytic CO_2 reduction activity, Small 13 (2017) 1603938.

[22] X. Huang, W. Gu, Y. Ma, D. Liu, N. Ding, L. Zhou, J. Lei, L. Wang, J. Zhang, Recent advances of doped graphite carbon nitride for photocatalytic reduction of CO_2: a review, Res. Chem. Intermed. 46 (2020) 5133–5164.

[23] C. Wang, Y. Zhao, H. Xu, Y. Li, Y. Wei, J. Liu, Z. Zhao, Efficient Z-scheme photocatalysts of ultrathin g-C_3N_4-wrapped Au/TiO_2-nanocrystals for enhanced visible-light-driven conversion of CO_2 with H_2O, Appl. Catal. B Environ. 263 (2020) 118314.

[24] C. Wang, Y. Hou, J. Cheng, M.J. Lin, X. Wang, Biomimetic donor-acceptor motifs in carbon nitrides: enhancing red-light photocatalytic selective oxidation by rational surface engineering, Appl. Catal. B Environ. 294 (2021), 120259.

[25] P. Roy, A. Jha, V.B. Yasarapudi, T. Ram, B. Puttaraju, S. Patil, J. Dasgupta, Ultrafast bridge planarization in donor-pi-acceptor copolymers drives intramolecular charge transfer, Nat. Commun. 8 (2017) 1716.

[26] H. Ou, X. Chen, L. Lin, Y. Fang, X. Wang, Biomimetic donor-acceptor motifs in conjugated polymers for promoting exciton splitting and charge separation, Angew. Chem. Int. Ed. 57 (2018) 8729–8733.

[27] J. Han, N. Li, D. Chen, Q. Xu, J. Lu, Boosting photocatalytic activity for porphyrin-based D-A conjugated polymers via dual metallic sites regulation, Appl. Catal. B Environ. 317 (2022), 121724.

[28] G. Zhang, G. Li, T. Heil, S. Zafeiratos, F. Lai, A. Savateev, M. Antonietti, X. Wang, Tailoring the grain boundary chemistry of polymeric carbon nitride for enhanced solar hydrogen production and CO_2 reduction, Angew. Chem. Int. Ed. 58 (2019) 3433–3437.

[29] J.C. Wang, C.X. Cui, Q.Q. Kong, C.Y. Ren, Z. Li, L. Qu, Y. Zhang, K. Jiang, Mn-doped g-C_3N_4 nanoribbon for efficient visible-light photocatalytic water splitting coupling with methylene blue degradation, ACS Sustain. Chem. Eng. 6 (2018) 8754–8761.

[30] S. Yao, B.Q. Sun, P. Zhang, Z.Y. Tian, H.Q. Yin, Z.M. Zhang, Anchoring ultrafine Cu_2O nanocluster on PCN for CO_2 photoreduction in water vapor with much improved stability, Appl. Catal. B Environ. 317 (2022), 121702.

[31] Z. Li, C. Kong, G. Lu, Visible photocatalytic water splitting and photocatalytic two-electron oxygen formation over Cu- and Fe-doped g-C_3N_4, J. Phys. Chem. C 120 (2016) 56–63.

[32] Z. Wang, E. Almatrafi, H. Wang, H. Qin, W. Wang, L. Du, S. Chen, G. Zeng, P. Xu, Cobalt single atoms anchored on oxygen-doped tubular carbon nitride for efficient peroxymonosulfate activation: simultaneous coordination structure and morphology modulation, Angew. Chem. Int. Ed. 134 (2022) e202202338.

[33] Y. Zeng, X. Liu, C. Liu, L. Wang, Y. Xia, S. Zhang, S. Luo, Y. Pei, Scalable one-step production of porous oxygen-doped g-C_3N_4 nanorods with effective electron separation for excellent visible-light photocatalytic activity, Appl. Catal. B Environ. 224 (2018) 1–9.

[34] S. Wu, H. Yu, S. Chen, X. Quan, Enhanced photocatalytic H_2O_2 production over carbon nitride by doping and defect engineering, ACS Catal. 10 (2020) 14380–14389.

[35] X. Wang, J. Meng, X. Zhang, Y. Liu, M. Ren, Y. Yang, Y. Guo, Controllable approach to carbon-deficient and oxygen-doped graphitic carbon nitride: robust photocatalyst against recalcitrant organic pollutants and the mechanism insight, Adv. Funct. Mater. 31 (2021) 2010763.

[36] Y. Yang, S. Wang, Y. Jiao, Z. Wang, M. Xiao, A. Du, Y. Li, J. Wang, L. Wang, An unusual red carbon nitride to boost the photoelectrochemical performance of wide bandgap photoanodes, Adv. Funct. Mater. 28 (2018) 1805698.

[37] Y. Zhu, Z. Chen, Y. Gao, C. Hu, General synthesis of carbon and oxygen dual-doped graphitic carbon nitride via copolymerization for non-photochemical oxidation of organic pollutant, J. Hazard. Mater. 394 (2020), 122578.

[38] Y. Chen, X. Liu, L. Hou, X. Guo, R. Fu, J. Sun, Construction of covalent bonding oxygen-doped carbon nitride/graphitic carbon nitride Z-scheme heterojunction for enhanced visible-light-driven H_2 evolution, Chem. Eng. J. 383 (2020), 123132.

[39] F. Wei, Y. Liu, H. Zhao, X. Ren, J. Liu, T. Hasan, L. Chen, Y. Li, B.L. Su, Oxygen self-doped g-C_3N_4 with tunable electronic band structure for unprecedentedly enhanced photocatalytic performance, Nanoscale 10 (2018) 4515–4522.

[40] T. Huang, S. Pan, L. Shi, A. Yu, X. Wang, Y. Fu, Hollow porous prismatic graphitic carbon nitride with nitrogen vacancies and oxygen doping: a high-performance visible light-driven catalyst for nitrogen fixation, Nanoscale 12 (2020) 1833–1841.

[41] P. Qiu, C. Xu, H. Chen, F. Jiang, X. Wang, R. Lu, X. Zhang, One step synthesis of oxygen doped porous graphitic carbon nitride with remarkable improvement of photo-oxidation activity: role of oxygen on visible light photocatalytic activity, Appl. Catal. B Environ. 206 (2017) 319–327.

[42] Z. Mo, X. Zhu, Z. Jiang, Y. Song, D. Liu, H. Li, X. Yang, Y. She, Y. Lei, S. Yuan, H. Li, L. Song, Q. Yan, H. Xu, Porous nitrogen-rich g-C_3N_4 nanotubes for efficient photocatalytic CO_2 reduction, Appl. Catal. B Environ. 256 (2019), 117854.

[43] X. Zhu, X. Yang, X. Zhu, J. Yuan, M. Zhou, X. She, Q. Yu, Y. Song, Y. She, Y. Hua, H. Li, H. Xu, Exploring deep effects of atomic vacancies on activating CO_2 photoreduction via rationally designing indium oxide photocatalysts, Chem. Eng. J. 422 (2021), 129888.

[44] D. Zhao, Y. Wang, C.L. Dong, Y.C. Huang, J. Chen, F. Xue, S. Shen, L. Guo, Boron-doped nitrogen-deficient carbon nitride-based Z-scheme heterostructures for photocatalytic overall water splitting, Nat. Energy 6 (2021) 388–397.

[45] J. Liu, Y. Liu, N.Y. Liu, Y.Z. Han, X. Zhang, H. Huang, Y. Lifshitz, S. Lee, J. Zhong, Z.H. Kang, Metal-free efficient photocatalyst for stable visible water splitting via a two-electron pathway, Science 347 (2021) 970–974.

[47] G. Kumari, X. Zhang, D. Devasia, J. Heo, P.K. Jain, Watching visible light-driven CO_2 reduction on a plasmonic nanoparticle catalyst, ACS Nano 12 (2018) 8330–8340.

[48] L. Zou, R. Sa, H. Zhong, H. Lv, X. Wang, R. Wang, Photoelectron transfer mediated by the interfacial electron effects for boosting visible-light-driven CO_2 reduction, ACS Catal. 12 (2022) 3550–3557.

[49] B. Li, F. Wei, B. Su, Z. Guo, Z. Ding, M.Q. Yang, S. Wang, Mesoporous cobalt tungstate nanoparticles for efficient and stable visible-light-driven photocatalytic CO_2 reduction, Mater. Today Energy 24 (2022), 100943.

[50] G. Yin, X. Huang, T. Chen, W. Zhao, Q. Bi, J. Xu, Y. Han, F. Huang, Hydrogenated blue titania for efficient solar to chemical conversions: preparation, characterization, and reaction mechanism of CO_2 reduction, ACS Catal. 8 (2018) 1009–1017.

[51] Z. Luo, X. Ye, S. Zhang, S. Xue, C. Yang, Y. Hou, W. Xing, R. Yu, J. Sun, Z. Yu, X. Wang, Unveiling the charge transfer dynamics steered by built-in electric fields in BiOBr photocatalysts, Nat. Commun. 13 (2022) 2230.